A chromospheric resonance cavity in a sunspot mapped with seismology

David B. Jess[1,2], Ben Snow[3], Scott J. Houston[1], Gert J. J. Botha[4], Bernhard Fleck[5], S. Krishna Prasad[1], Andrés Asensio Ramos[6,7], Richard J. Morton[4], Peter H. Keys[1], Shahin Jafarzadeh[8,9], Marco Stangalini[10,11], Samuel D. T. Grant[1] & Damian J. Christian[2]

[1]*Astrophysics Research Centre, School of Mathematics and Physics, Queen's University Belfast, Belfast BT7 1NN, U.K.*

[2]*Department of Physics and Astronomy, California State University Northridge, Northridge, CA 91330, U.S.A.*

[3]*Centre for Geophysical and Astrophysical Fluid Dynamics, University of Exeter, Exeter, EX4 4QF, U.K.*

[4]*Department of Mathematics, Physics and Electrical Engineering, Northumbria University, Newcastle upon Tyne, NE1 8ST, U.K.*

[5]*ESA Directorate of Science, Operations Department, c/o NASA/GSFC Code 671, Greenbelt, MD 20071, U.S.A.*

[6]*Instituto de Astrofísica de Canarias, C/Vía Lactea s/n, E-38205 La Laguna, Tenerife, Spain*

[7]*Departamento de Astrofísica, Universidad de La Laguna, E-38206 La Laguna, Tenerife, Spain*

[8]*Institute of Theoretical Astrophysics, University of Oslo, P.O. Box 1029 Blindern, NO-0315 Oslo, Norway*

[9]*Rosseland Centre for Solar Physics, University of Oslo, P.O. Box 1029 Blindern, N-0315 Oslo, Norway*

[10]*Italian Space Agency (ASI), Via del Politecnico snc, 00133 Roma, Italy*

[11]*INAF-OAR National Institute for Astrophysics, Via Frascati 33, 00078 Monte Porzio Catone (RM), Italy*

Sunspots are intense collections of magnetic fields that pierce through the Sun's photosphere, with their signatures extending upwards into the outermost extremities of the solar corona[1]. Cutting-edge observations and simulations are providing insights into the underlying wave generation[2], configuration[3,4], and damping[5] mechanisms found in sunspot atmospheres. However, the *in-situ* amplification of magnetohydrodynamic waves[6], rising from a few hundreds of m/s in the photosphere to several km/s in the chromosphere[7], has, until now, proved difficult to explain. Theory predicts that the enhanced umbral wave power found at chromospheric heights may come from the existence of an acoustic resonator[8–10], which is created due to the substantial temperature gradients experienced at photospheric and transition region heights[11]. Here we provide strong observational evidence of a resonance cavity existing above a highly magnetic sunspot. Through a combination of spectropolarimetric inversions and comparisons with high-resolution numerical simulations, we provide a new seismological approach to map the geometry of the inherent temperature stratifications across the diameter of the underlying sunspot, with the upper boundaries of the chromosphere ranging between 1300 ± 200 km and 2300 ± 250 km. Our findings will allow the three-dimensional structure of solar active regions to be conclusively determined from relatively commonplace two-dimensional Fourier power spectra. The techniques presented are also readily suitable for investigating temperature-dependent resonance effects in other areas of astrophysics, in-

cluding the examination of Earth-ionosphere wave cavities[12].

Spectropolarimetric observations, captured in the Si I 10827 Å and He I 10830 Å lines at high spatial (110 km per pixel), temporal (14.6 s) and spectral (0.04 Å per pixel) resolution, were acquired across the centre of a large sunspot on 14 July 2016 using the Facility Infrared Spectropolarimeter[13] (FIRS) at the Dunn Solar Telescope. Simultaneous contextual imaging is provided by the Rapid Oscillations in the Solar Atmosphere[14] (ROSA) and the Interferometric BIdimensional Spectrometer[15] (IBIS) instruments. Spatially resolved Doppler velocities are derived as a function of time for the entire 86 minute data sequence, providing 35,350 individual velocity measurements with amplitudes in the range of $\pm$0.3 km/s and $\pm$6 km/s for the photospheric Si I 10827 Å and upper-chromospheric He I 10830 Å time series, respectively. The resulting images and spectra (Fig. 1) highlight the persistent and regular wave signatures manifesting in the sunspot umbra.

A long-lived filamentary structure, consistent with previous observational studies[16,17], naturally segregates the sunspot into two distinct umbrae (Fig. 1). The centres of gravity (or barycenters) of each isolated umbra are calculated, allowing the wave characteristics to be studied as a function of distance from their respective umbral core. Fourier spectral energies[18] are computed for each of the 101 spatial pixels crossing the sunspot umbrae (Fig. 2), revealing distinct differences between the upper-chromospheric He I 10830 Å spectra and their co-spatial photospheric Si I 10827 Å counterparts. Most notable is the fact that all of the He I 10830 Å spectral energies can be categorised by three distinct regions: (region I; <5 mHz) the evanescent regime with frequencies

below the acoustic cut-off, (region II; $6 - 17$ mHz) the region where propagating waves become permissible and demonstrate broad spectral peaks and strong spectral energies that are consistent with previous observational findings[19], and (region III; $18 - 27$ mHz) the final regime where the spectral energy demonstrates a steep power-law relationship with gradient α. It is region III that acts as both an indicator for the presence of a resonant layer[9], as well as the ability to use the spectral slope, α, as a diagnostic tool for estimating the thickness of the temperature structuring of the chromospheric resonance cavity[11].

Fitting the He I 10830 Å spectral energy gradients for region III through maximum-likelihood statistical approaches[20] reveals a strong correspondence between the steepness of the slope and the distance subtended from the corresponding umbral barycenter (Fig. 3). While the spectral gradients for region II remain consistent across the entire extent of the sunspot (with characteristic spectral gradients of -2.1 ± 0.2), the spectral slopes for region III vary as a function of distance from their respective umbral barycenter, with gradients as shallow as -5.4 ± 0.6 at the core of the relevant umbra, extending to gradients as steep as -7.8 ± 0.6 at maximal distances ($\sim$3000 km) from each barycenter. Spectral slopes of this magnitude closely resemble the strong dissipative ranges previously documented in studies of the solar wind[21].

To compare with the observational findings, the Lare2D[22] numerical non-linear compressible MHD code, which is employed in a 1.5D configuration, is driven by the photospheric velocity profiles extracted from the observational Si I 10827 Å Doppler shifts and allowed to evolve in time. The embedded atmospheric model is constrained by HAnle and Zeeman Light[23] (HAZEL)

inversions applied to the spectropolarimetric data products[24], with the computed velocity signals extracted with a cadence of 14.6 s (to match that of the FIRS observations) following propagation of the wave signatures to the upper temperature gradient corresponding to the commencement of the transition region, which is consistent with the predicted formation height of the He I 10830 Å spectral line[25]. The velocity time series is cropped to 86 minutes in duration to match that of the observations and converted into spectral energies (Fig. 2e,f). This process is repeated for input atmospheres scaled to 80%, 90%, 110% and 120% of the original temperature stratification height, providing resonance cavity depths (photosphere to the base of the transition region) spanning $1700 - 2545$ km. The spectral energies computed for both the modelled and observed time series show similar trends across regions I, II and III (Fig. 2). In particular, the modelled region III demonstrates an identical rise in spectral energy at $\sim$20 mHz, before dropping off very rapidly with increasing frequency. Importantly, re-running the numerical simulations for an atmospheric profile devoid of the steep transition region temperature gradient produces spectral energies where the secondary $\sim$20 mHz spectral peak is absent. This verifies that the steep temperature gradient intrinsic to the solar transition region, which amplifies the spectral energies at $\sim$20 mHz, is required for the initiation of resonance behaviour. The maximum-likelihood fitted spectral slopes for region III reveals that shallower spectral gradients correspond to inherently deeper chromospheric cavities (Fig. 3b), allowing the observed spectral slopes for region III to unveil the cavity depths of the local sunspot atmosphere. Importantly, a larger cavity depth introduces a greater resonant energy content, hence providing more energy across the frequency range, and thus reducing the steepness of the associated spectral slope[11].

The range of gradients measured for region III ($18-27$ mHz) of the sunspot spectral energies span -5.4 ± 0.6 (close to the umbral barycenter) to -7.8 ± 0.6 (at the outermost extremities of the umbra), suggesting that the chromospheric resonance cavity is thickest near the core of the umbra, dropping to its thinnest depth at the penumbral boundary (Fig. 3). The upper geometric height of the chromosphere, $\tau_{\rm chromo}$, which corresponds to the uppermost boundary of the resonance cavity before the commencement of the transition region, can be defined (Fig. 3b) as,

$$\tau_{\rm chromo}\,({\rm km}) = \frac{\text{Region III spectral slope} + 26.408}{0.009131}\cos\theta\,, \tag{1}$$

where θ is the inclination angle of the wave propagation path with respect to the normal to the solar surface. Use of the inclination angle is important since the Lare2D numerical code simulates the wave evolution along a given magnetic field line, which may be inclined with respect to the solar normal. Hence, taking the magnetic field inclinations into consideration allows for the conversion of a wave propagation distance into a true geometric height of the chromosphere for that particular spatial location. Utilising the vector magnetic fields derived from HAZEL inversions[24] yields inclination angles ranging from 0 degrees at the umbral barycenters, through to approximately 50 degrees towards the outer umbral boundaries, providing geometric heights for the upper chromosphere on the order of 2300 ± 250 km and 1300 ± 200 km for the umbral cores and umbral/penumbral boundaries, respectively (Fig. 4).

Here, we show strong evidence substantiating the presence of a chromospheric resonance cavity above a sunspot. We reveal how high resolution spectropolarimetric observations, when combined with cutting-edge numerical MHD simulations, provide the spectral energy sensitivity necessary to accurately measure the high-frequency spectral gradients that are modulated by the

depth of the chromospheric resonance cavity. Importantly, the variable cavity depths across the diameter of the sunspot have important implications for atmospheric seismology, since the umbral atmosphere can no longer be considered as a homogeneous slab environment. Instead, thicknesses of the chromospheric resonance layer will need to be incorporated into seismological estimations in order to improve the accuracy of such techniques. Looking ahead, fiber-fed spectrographs on the upcoming 4m Daniel K. Inouye Solar Telescope will provide two-dimensional spectral energy maps of sunspots with unprecedented resolving power, allowing revolutionary three-dimensional atmospheric reconstructions to be uncovered.

Furthermore, the topic of resonance cavities is fundamentally important across a wide range of ongoing astrophysical research including, but not limited to, the examination of near-Earth ionospheric wave cavities[12]. As a result, understanding the physics responsible for the creation of resonance cavities, along with their impact on the universe around us, is of paramount importance. Our results enable the astrophysical community to benchmark, through novel seismological approaches, what atmospheric characteristics are required to form a stable resonance cavity (e.g., specific temperature stratifications), what impact this has on waveforms interacting with the cavity structure (e.g., power enhancements at well-defined frequencies), and how cutting-edge numerical simulations can be employed alongside high-precision spectropolarimetric data products to deduce physical parameters corresponding to the local plasma conditions (e.g., cavity depth).

1. Borrero, J. M. & Ichimoto, K. Magnetic Structure of Sunspots. *Living Reviews in Solar Physics* **8**, 4 (2011).

2. Bogdan, T. J. *et al.* Waves in the Magnetized Solar Atmosphere. II. Waves from Localized Sources in Magnetic Flux Concentrations. *Astrophys. J.* **599**, 626–660 (2003).

3. Lites, B. W., Thomas, J. H., Bogdan, T. J. & Cally, P. S. Velocity and Magnetic Field Fluctuations in the Photosphere of a Sunspot. *Astrophys. J.* **497**, 464–482 (1998).

4. Nagashima, K. *et al.* Observations of Sunspot Oscillations in G Band and CaII H Line with Solar Optical Telescope on Hinode. *Publ. Astron. Soc. Jpn* **59**, S631–S636 (2007).

5. Grant, S. D. T. *et al.* Alfvén wave dissipation in the solar chromosphere. *Nature Physics* **14**, 480–483 (2018).

6. Kobanov, N. I. & Makarchik, D. V. Propagating waves in the sunspot umbra chromosphere. *Astron. Astrophys.* **424**, 671–675 (2004).

7. Tziotziou, K., Tsiropoula, G., Mein, N. & Mein, P. Dual-line spectral and phase analysis of sunspot oscillations. *Astron. Astrophys.* **463**, 1153–1163 (2007).

8. Hollweg, J. V. A new resonance in the solar atmosphere. I. Theory. *Sol. Phys.* **62**, 227–240 (1979).

9. Botha, G. J. J., Arber, T. D., Nakariakov, V. M. & Zhugzhda, Y. D. Chromospheric Resonances above Sunspot Umbrae. *Astrophys. J.* **728**, 84 (2011).

10. Felipe, T. Origin of the chromospheric three-minute oscillations in sunspot umbrae. *A&A* **627**, A169 (2019).

11. Snow, B., Botha, G. J. J. & Régnier, S. Chromospheric seismology above sunspot umbrae. *Astron. Astrophys.* **580**, A107 (2015).

12. Toledo-Redondo, S., Salinas, A., Fornieles, J., Portí, J. & Lichtenegger, H. I. M. Full 3-D TLM simulations of the Earth-ionosphere cavity: Effect of conductivity on the Schumann resonances. *Journal of Geophysical Research (Space Physics)* **121**, 5579–5593 (2016).

13. Jaeggli, S. A. *et al.* FIRS: a new instrument for photospheric and chromospheric studies at the DST. *Mem. Soc. Astron. Italiana* **81**, 763 (2010).

14. Jess, D. B. *et al.* ROSA: A High-cadence, Synchronized Multi-camera Solar Imaging System. *Sol. Phys.* **261**, 363–373 (2010).

15. Cavallini, F. IBIS: A New Post-Focus Instrument for Solar Imaging Spectroscopy. *Sol. Phys.* **236**, 415–439 (2006).

16. Socas-Navarro, H., McIntosh, S. W., Centeno, R., de Wijn, A. G. & Lites, B. W. Direct Imaging of Fine Structure in the Chromosphere of a Sunspot Umbra. *Astrophys. J.* **696**, 1683–1688 (2009).

17. Beck, C., Choudhary, D. P. & Rezaei, R. A Three-dimensional View of the Thermal Structure in a Super-penumbral Canopy. *Astrophys. J.* **788**, 183 (2014).

18. Stull, R. *An Introduction to Boundary Layer Meteorology*. Atmospheric and Oceanographic Sciences Library (Springer Netherlands, 2012).

19. Reznikova, V. E., Shibasaki, K., Sych, R. A. & Nakariakov, V. M. Three-minute Oscillations above Sunspot Umbra Observed with the Solar Dynamics Observatory/Atmospheric Imaging Assembly and Nobeyama Radioheliograph. *Astrophys. J.* **746**, 119 (2012).

20. Barret, D. & Vaughan, S. Maximum Likelihood Fitting of X-Ray Power Density Spectra: Application to High-frequency Quasi-periodic Oscillations from the Neutron Star X-Ray Binary 4U1608-522. *Astrophys. J.* **746**, 131 (2012).

21. He, J., Wang, L., Tu, C., Marsch, E. & Zong, Q. Evidence of Landau and Cyclotron Resonance between Protons and Kinetic Waves in Solar Wind Turbulence. *Astrophys. J. Lett.* **800**, L31 (2015).

22. Arber, T. D., Longbottom, A. W., Gerrard, C. L. & Milne, A. M. A Staggered Grid, Lagrangian-Eulerian Remap Code for 3-D MHD Simulations. *Journal of Computational Physics* **171**, 151–181 (2001).

23. Asensio Ramos, A., Trujillo Bueno, J. & Landi Degl'Innocenti, E. Advanced Forward Modeling and Inversion of Stokes Profiles Resulting from the Joint Action of the Hanle and Zeeman Effects. *Astrophys. J.* **683**, 542–565 (2008).

24. Houston, S. J. *et al.* The Magnetic Response of the Solar Atmosphere to Umbral Flashes. *Astrophys. J.* **860**, 28 (2018).

25. Avrett, E. H., Fontenla, J. M. & Loeser, R. Formation of the Solar 10830 Angstrom Line. In Rabin, D. M., Jefferies, J. T. & Lindsey, C. (eds.) *Infrared Solar Physics*, vol. 154 of *IAU Symposium*, 35 (1994).

Acknowledgements D.B.J. would like to thank the UK Science and Technology Facilities Council (STFC) for an Ernest Rutherford Fellowship, in addition to a dedicated standard grant which allowed this project to be undertaken. D.B.J. and S.D.T.G. also wish to thank Invest NI and Randox Laboratories Ltd. for the award of a Research & Development Grant (059RDEN-1) that allowed the computational techniques employed to be developed. B.S. is supported by STFC research grant ST/R000891/1. S.K.P. wishes to thank the UK STFC for support. A.A.R. is grateful to the Spanish Ministry of Economy and Competitiveness through project AYA2014-60476-P. S.J. acknowledges support from the European Research Council under the European Unions Horizon 2020 research and innovation program (grant agreement No. 682462) and from the Research Council of Norway through its Centres of Excellence scheme (project No. 262622). M.S. is grateful for funding received from the European Research Council under the European Unions Horizon 2020 Framework Programme for Research and Innovation, grant agreements H2020 PRE-EST (no. 739500) and H2020 SOLARNET (no. 824135), in addition to support from INAF Istituto Nazionale di Astrofisica (PRIN-INAF-2014). D.J.C. would like to thank California State University Northridge for start-up funding. The Dunn Solar Telescope at Sacramento Peak/NM was operated by the National Solar Observatory (NSO). NSO is operated by the Association of Universities for Research in Astronomy (AURA), Inc., under cooperative agreement with the National Science Foundation (NSF). The SDO/AIA imaging employed in this work are courtesy of NASA/SDO and the AIA, EVE, and HMI science teams. The authors wish to acknowledge scientific discussions with the Waves in the Lower Solar Atmosphere (WaLSA; www.WaLSA.team) team, which is supported by the Research Council of Norway (project number 262622). Imagery produced by the Visualization and Analysis Platform for atmospheric, Oceanic and solar Research (VAPOR; www.vapor.ucar.edu), a product of the Computational Information Systems Laboratory at the National Center for Atmospheric Research.

Author Contributions D.B.J. and D.J.C. designed the observational instrumentation setup. D.B.J., S.J.H. and S.K.P. undertook the ground-based observations. D.B.J, S.J.H., A.A.R. and S.D.T.G. performed analysis of the observations. B.S. and G.J.J.B. designed and carried out numerical MHD simulations. D.B.J., B.S., S.J.H., G.J.J.B., S.K.P., P.H.K., S.J., M.S., B.F. and R.J.M. interpreted the observations and simulations. D.B.J., B.S., S.J.H., R.J.M. and S.D.T.G. prepared and processed all data products. All authors discussed the results and commented on the manuscript.

Competing Interests The authors declare that they have no competing financial interests.

Correspondence Correspondence and requests for materials should be addressed to David B. Jess (email: d.jess@qub.ac.uk).

Methods

Observations. The sunspot at the centre of the active region NOAA 12565 on 14 July 2016 was the primary focus of the observing campaign. The image sequence duration was approximately 86 minutes, and was obtained during excellent seeing conditions between 13:42 – 15:08 UT with the Dunn Solar Telescope at Sacramento Peak, New Mexico. The Hydrogen-Alpha Rapid Dynamics camera[26] (HARDcam) and Rapid Oscillations in the Solar Atmosphere[14] (ROSA) imaging systems were simultaneously used to capture active region NOAA 12565 at G-band, blue continuum (4170 Å), Ca II K and Hα wavelengths, which was positioned at heliocentric co-ordinates ($-582''$, $30''$), providing a heliocentric viewing angle of 38° ($\mu \simeq 0.79$). This location corresponds to N05.2E38.1 in the conventional heliographic co-ordinate system. To complement the ROSA and HARDcam data streams, the Facility Infrared Spectropolarimeter[13] (FIRS) slit-based spectrograph and Interferometric BIdimensional Spectrometer[15] (IBIS) imaging spectrograph acquired contemporaneous observations of the same active region in the He I 10830 Å and Ca II 8542 Å spectral lines, respectively.

The FIRS instrument was configured to obtain diffraction-limited spectropolarimetry of the He I 10830 Å upper-chromospheric absorption lines by utilising a $75''$ slit length (providing a spatial sampling of $0''.15$ per pixel along the slit), combined with a $0''.225$ slit width. A confined five-step raster was obtained by moving the slit $0''.225$ after each integration, providing a narrow $75'' \times 1''.125$ slot-type field of view that passed through the centre of the umbral core. Each spectrum obtained consisted of 12 consecutive additions of the modulation states to increase the signal-to-noise of the relevant Stokes profiles, providing a final cadence equal to 14.6 s. The observations

were reduced into science-ready data products using the publicly available National Solar Observatory FIRS pipeline[27], ultimately providing a spectral sampling of 0.04 Å for the He I 10830 Å spectra. To assist with the determination of the FIRS slit pointing and alignment, a slit-jaw camera (in sync with the acquisition of each spectrum) was employed alongside the ROSA, HARDcam and IBIS image sequences to allow the precise spatial location and orientation of the FIRS slit to be mapped.

The IBIS system was deployed in imaging mode (i.e., no spectropolarimetric information was retrieved) to increase the field of view captured and to decrease the time taken to acquire a spectral scan. A total of 47 discrete, non-equidistant wavelength steps were utilised across the Ca II 8542 Å line profile with a spatial sampling of $0\farcs098$ per pixel, providing a circular field of view with a diameter of $97''$ and a spectral coverage of $8540.82 - 8543.42$ Å (i.e., line core ± 1.3 Å). In total, 543 imaging spectral scans were completed, each with a cadence of 9.4 s. A radial blueshift correction was performed to compensate for the classically mounted etalons[28]. A whitelight camera, in sync with the IBIS narrowband sequences, was employed to de-stretch the resulting spectral scans[29,30]. Contextual ROSA 4170 Å continuum and IBIS Ca II 8542 Å line core images are displayed in Fig. 1, alongside contours depicting the precise location of the FIRS slit.

Establishing the Doppler velocities. The orientation of the FIRS slit resulted in it crossing an approximate 11 Mm ($\sim 15''$) expanse of the sunspot umbra. This extent is highlighted by a solid green line in Fig. 1b, with pixels beyond this corresponding to penumbral or quiet Sun locations. Each Stokes I spectrum extracted from the sunspot umbra is normalised by its own respective average continuum intensity, I_c (Extended Data Fig. 1a). When the time-spectral evolution of an

umbral pixel is examined (see, e.g., Extended Data Fig. 1b), it is clear to see regular periodic wave signals with a characteristic period on the order of 3 minutes.

It must be noted that the He I spectral window around 10830 Å is actually a collection of three independent electron transitions:[31] $2s^3S_1$ – $2p^3P_0$ at 10829.09 Å, $2s^3S_1$ – $2p^3P_1$ at 10830.25 Å, and $2s^3S_1$ – $2p^3P_2$ at 10830.34 Å. Typically, under conditions where velocity signatures are significantly subsonic,[32,33] the He I triplet is observed as two absorption features since the 10830.25 Å and 10830.34 Å profiles are fully blended together (forming the deep "red" component), while the more shallow "blue" component at 10829.09 Å remains isolated[34]. It is common practice to perform spectropolarimetric inversions on the blue He I component since it has a higher effective Landé g-factor ($g_{\rm eff} = 2.0$ at 10829.09 Å, versus $g_{\rm eff} = 1.75$ and $g_{\rm eff} = 1.25$ at 10830.25 Å and 10830.34 Å, respectively) and potential blends do not need to be considered. Indeed, the HAZEL inversions performed on this dataset were applied to the blue He I component[24]. On the other hand, (subsonic) Doppler velocity measurements can be derived more reliably from the red He I component due to its significantly larger line depth and intrinsically better signal-to-noise. For the purpose of establishing Doppler maps of the sunspot umbra, we fit the red component of the He I spectra since the resulting profiles are fully blended, with no evidence of supersonic flows (see, e.g., Extended Data Fig. 1a).

By fitting all 35,350 (101 pixels across the 11 Mm umbral diameter and 350 acquisitions in time) He I 10830 Å absorption lines with a Voigt profile[35] (a combination of Gaussian and Lorentzian profiles due to the Doppler and pressure broadening sensitivities, respectively, of the He I 10830 Å line), the intrinsic Doppler velocities were mapped. Velocity oscillations with am-

plitudes in the range of ± 6 km s^{-1}, were found to span the entire diameter of the chromospheric sunspot umbra and last throughout the duration of the observing period (see, e.g., Extended Data Fig. 1b).

Segregating the umbra into two distinct regions. Within the 11 Mm umbral region, there existed a persistent brightening that was only visible in the chromospheric image sequences obtained by IBIS (Ca II 8542 Å) and HARDcam (Hα 6563 Å). The brightening, at approximately 5.6 Mm ($\approx$7.7″) along the umbral portion of the FIRS slit, is highlighted with a pink cross in Fig. 1b and in Extended Data Fig. 2a. Due to an absence of this feature in the photospheric observations (see, e.g., the ROSA 4170 Å continuum image depicted in Fig. 1a), the chromospheric umbral brightening is likely to be a long-lived filamentary structure[16,36]. Indeed, from inspection of the time-distance map of the fitted He I Doppler velocities in Extended Data Fig. 1b, the umbral brightening (highlighted using a vertical dashed pink line) exhibits preferential red-shifted Doppler velocities, a characteristic that is consistent with previous observational measurements[17]. Extended Data Fig. 2b displays a magnified view of the chromospheric sunspot umbra, where the persistent brightening is better revealed (and highlighted using a pink cross).

To focus our study purely on the umbral signatures, we decompose the umbral spectra into two distinct regions that are isolated from one another by the long-lived chromospheric filamentary structure crossing the FIRS slit. To do this, we extract a time-averaged Stokes I/I_c intensity along the umbral portion of the FIRS slit (see, e.g., the solid green line in Extended Data Fig. 2b) that corresponds to the He I 10830 Å line core. This intensity profile is plotted in Extended Data Fig. 2c, where the vertical dashed pink line highlights the location of the persistent chromospheric umbral

brightening, which demonstrates intensities considerably above the quiescent umbral background. Next, the centres of gravity (or barycenter) for the intensity profile south (i.e., <5.6 Mm) and north (i.e., >5.6 Mm) of the umbral brightening are calculated to be 2.8 Mm and 8.3 Mm, respectively, which are represented by the vertical dashed red lines in Extended Data Fig. 2c. Thus, the green and blue shaded regions in Extended Data Fig. 2c represent the southern and northern umbral regions, respectively, which are isolated from one another by the persistent chromospheric umbral brightening. Now, any signatures extracted from the data can be related directly to a particular umbral region for further characterisation, in addition to the distance from their respective umbral barycenter.

Regions present in the Fourier spectra. In accordance with recent theoretical work[11], we isolate the spectral energy plots into three distinct regions:

- Region I (<5 mHz) – Part of the spectral energy that is governed by the local acoustic cut-off frequency, ω_c, which only allows waves to propagate upwards providing,

$$\omega > \omega_c = \frac{c_s}{2H}\sqrt{1 + 2\frac{\delta H}{\delta z}} \, ,$$

  where c_s is the local sound speed, z is the atmospheric height and $H = c_s^2/(\gamma g)$ with γ the adiabatic index and g the acceleration due to gravity[37,38]. Due to the almost vertical nature of the magnetic field lines at the core of the sunspot umbra[24], we choose an upper limit for region I at 5 mHz, which is consistent with other sunspot observations[39].

- Region II ($6 - 17$ mHz) – Portion of the spectral energy where propagating waves become permissible (i.e., >5 mHz) and demonstrate broad spectral peaks and strong spectral energies

that are consistent with previous observational findings[19,40,41]. Here, region II continues from $6-17$ mHz (allowing for a buffer region between $5-6$ mHz to allow the overall spectrum to reach a peak energy), revealing a gradual decrease in the spectral energy with frequency. The upper boundary of region II is set at 17 mHz, since another peak at frequencies beyond 18 mHz commences the beginning of region III.

- Region III ($18-27$ mHz) – The final regime of the spectral energy corresponds to the range where steep spectral gradient declines are found. This is the region where the spectral energy is proportional to a f^{α} scaling, where f is the frequency and α is the linear gradient when plotted on log–log axes[11]. Due to the 14.6 s cadence of the FIRS observations, the resulting Nyquist frequency is 34 mHz. From examination of the individual spectral energies, white noise fluctuations commence around $28-30$ mHz, which was identified by the flattening of the spectral energy beyond these frequencies (see Fig. 2d). As a result, we set the upper boundary for region III at 27 mHz to avoid contamination from high-frequency white noise. It is region III that acts as a diagnostic tool for estimating the thickness and temperature structuring of the chromospheric resonance cavity.

It must be noted that the spectral frequency ranges for regions I (<5 mHz), II ($6-17$ mHz) and III ($18-27$ mHz) remain fixed throughout the data analyses.

Features visible in the spectral energy maps. Fig. 2d displays the spectral energies for all 101 pixels across the sunspot using a graduated blue-to-pink colour scale. While there is scatter in the spectral energy at each component frequency, the general trend remains the same across all umbral

pixels, reiterating the usefulness of sub-dividing the spectral energy densities into their constituent regions (i.e., regions I, II and III). The mean spectral energy is overplotted in Fig. 2d using a solid black line, along with the maximum-likelihood fitted lines of best fit for regions II and III using solid red lines. It is clear to see that, on average, the maximum-likelihood fitted spectral gradient for region III is steeper than that for region II, as predicted in recent theoretical models[11].

It is possible to re-display Fig. 2d, only now preserving the information along the spatial diameter of the chromospheric sunspot umbra. Extended Data Fig. 3 displays a two-dimensional map of the spectral energy, plotted as a function of frequency (x-axis) and distance across the umbra (y-axis). As with the spectral energies plotted in Fig. 2d, it is clear to see a dominant broad band of peak power at $\approx$5 mHz across the entirety of the umbra. From visual inspection, it is also possible to identify wedge-shaped traces of peak power extending outwards from the north and south umbral barycenters (identified by the horizontal dashed green lines). A black dotted line in Extended Data Fig. 3 tracks the frequency corresponding to the weighted spectral energy centroid (between frequencies of $3 - 17$ mHz) across the entirety of the sunspot umbra. It can be seen that at the north/south umbral barycenters correspond to the highest centroid frequency ($\sim$6.5 mHz or $\sim$155 s), while the furthest extremities of each umbral section demonstrate the lowest centroid frequencies ($\sim$5.0 mHz or $\sim$180 s). This type of behaviour is consistent with the umbral barycenters displaying the most vertical magnetic fields, hence pushing the acoustic cut-off frequency to higher values[37]. A similar phenomenon has also been observed in IBIS spectral imaging observations of umbral oscillations[39], and reiterates the appropriateness of defining the start of region II at 6 mHz.

From Extended Data Fig. 3, it is also possible to identify the second enhancement of spectral energy corresponding to region III (≈ 18 mHz or 55 s). Here, there appears to be more pronounced enhancements of spectral energy close to the north/south umbral barycenters (i.e., coincident with the horizontal dashed green lines in Extended Data Fig. 3), when compared to similar frequencies at the very extreme edges of the sunspot umbra (e.g., distances of approximately 0 Mm and 11 Mm in Extended Data Fig. 3). The spectral energy associated with region III is much weaker than that found in region II, often by $1-2$ orders of magnitude (also visible in Fig. 2d). As the spectral gradient present in region III contains information related to the structuring of the underlying umbral resonance cavity, it is important to calculate the spectral slope with a high degree of precision.

Fitting the spectral energy gradients. To calculate the spectral slopes corresponding to regions II and III, maximum-likelihood fitted gradients are computed for each of the 101 spectral energies across the chromospheric umbra. Often linear lines of best fit are established to determine the spectral slopes of Fourier power spectra[42]. However, the weighted least-squares minimisation process assumes that the data to be fitted are normally (Gaussian) distributed[20], which may not necessarily be the case, especially when the periodogram of a stationary, linear stochastic process naturally follows a χ^2_2 distribution[43,44]. As a result, we apply the maximum-likelihood approach[20], which has recently been successfully applied to solar wave studies[45], to calculate the spectral gradients for regions II and III of the 101 spectral energies across the diameter of the sunspot umbra. The spectral gradients for regions II and III, as a function of distance from their respective umbral barycenter, are plotted in Fig. 3a. It is clear that the spectral slopes for region II are relatively constant, with a slope of -2.1 ± 0.2. Contrarily, the spectral gradients for region III are seen to

vary as a function of distance from their respective umbral barycenter, with gradients as shallow as -5.4 ± 0.6 at the core of the relevant umbra, extending to gradients as steep as -7.8 ± 0.6 at maximal distances ($\sim$3000 km) from each barycenter.

We believe the gradients displayed for region II in Fig. 3a point towards a universal sunspot characteristic for waves detected in chromospheric spectral lines. A recent observational examination of the spectral power slopes for an entirely different sunspot, using ground-based images obtained in the Ca II K and Hα line cores, found similar spectral gradients (within the $6 - 17$ mHz spectral range) to those presented here[42]. These gradients are steeper than both the f^{-1} and $f^{-5/3}$ relationships that would be expected for granulation (i.e., pink) noise patterns[46] and the Kolomogorov inertial range[47], respectively. Instead, they more closely resemble the f^{-2} red noise that is linked to the strong viscous dissipative regimes associated with Brownian motion[48]. Region III, on the other hand, has even steeper spectral gradients that more closely resemble the strong dissipative ranges previously documented in studies of the solar wind[21,49]. Importantly, the steepening of the spectral slopes as one moves away from the umbral barycenters indicates a strong dependency between the value of the spectral gradient and the characteristics of the underlying resonance cavity in which the spectral signatures were generated.

Numerical magnetohydrodynamic simulations. The numerical code employed in the current work is based on the well-documented Lare2D[22] software. Here, a velocity driver is injected into an atmospheric model, containing realistic temperature and density structuring, allowing the Lare2D code to evolve the idealised non-linear compressible MHD equations to compute the velocity signatures as a function of distance along the computational domain. The numerical domain

covers the vertical range -21 Mm $\leq z \leq 21$ Mm and is resolved by 8192 grid cells. The upper convection zone is modelled by a polytropic temperature profile and situated at $z < 0$ Mm in the domain. Above $z = 0$ Mm the temperature profile of sunspot model[50] 'M' is used, which connects smoothly at the transition region with a typical coronal temperature profile[51]. Near the upper boundary the temperature profile is flattened (i.e., a constant value is used) to create an open boundary at $z = 21$ Mm. An initial equilibrium is obtained by solving the pressure balance equation, and the two horizontal directions of the computational domain are invariant, making the resulting simulation 1.5D.

In order to make the numerical outputs as realistic as possible, we employ the HAZEL inversions of the umbral barycenter pixels (i.e., where the magnetic field inclination angles are approximately 0 degrees) of active region NOAA 12656 [ref. 24] to provide chromospheric plasma constraints, which allow the sunspot model[50] 'M' to be re-scaled across the rest of the computational grid. This re-sampled sunspot model formed the background atmosphere embedded within the Lare2D code, with the temperature values plotted using a solid black line in Extended Data Fig. 4. It must be noted that the sunspot under current investigation is slightly less magnetic and fractionally hotter than the standard sunspot model[50] 'M' atmosphere. Comparisons with the outputs of the Very Fast Inversion of the Stokes Vector[52] (VFISV) algorithm, applied to co-temporal SDO/HMI vector magnetogram data[53] that have a formation height in the low photosphere, reveal maximum umbral magnetic field strengths on the order of 2000 G, which is consistent with the re-sampled sunspot models.

Previous theoretical work[11] that studied the characteristics of sunspot resonance cavities em-

ployed a variety of injected photospheric velocity drivers, including those corresponding to white (f^0), pink (f^{-1}) and red (f^{-2}) noise signatures, which are believed to be representative of the spectral signatures present in the Sun's upper convection zone[54]. However, the spectroscopic observations of active region NOAA 12565 obtained by FIRS allows us to provide a better estimate of the real underlying photospheric velocity signal. Extracting bisector velocities of the Si I 10827 Å absorption feature at 20% of the maximum line depth provide photospheric velocities that correspond to an optical depth of $\log(\tau_{500\mathrm{nm}}) \sim -0.65$, or $\sim$50 km above the photospheric layer[50,55]. The extracted Si I 10827 Å velocity signatures have peak amplitudes on the order of 300 m/s (see the Fig. 2a), which is consistent with previous sunspot oscillation studies[56]. These photospheric velocity perturbations are re-scaled and applied at the lower ($z = -21$ Mm) boundary of the Lare2D code and allowed to evolve. The re-scaling is to ensure that the wave root mean square (rms) amplitudes produced by the simulations at $z = 0$ Mm (i.e., the photosphere) are consistent with the observed Si I 10827 Å profile fluctuations.

Data interpretation The velocity outputs from the Lare2D simulation were extracted at a cadence of 14.6 s (to match that of the FIRS observations) at an atmospheric height of 2120 km (vertical dotted black line in Extended Data Fig. 4), which is consistent with the approximate formation height of the He I 10830 Å spectral line[25,57]. The velocity time series was then cropped to 86 minutes in duration (again, to match that of the observations) and converted into spectral energies by following the same methodology applied to the FIRS He I 10830 Å data. There are a number of distinct similarities between the observed and simulated velocity time series (Fig. 2c,e). First, both the observed and simulated time series appear modulated by a long-term trend. Such long-

period modulation has been extensively observed in magnetoacoustic wave studies[58–60], which is normally explained as a consequence of beat phenomena created by the superposition of a number of closely spaced frequencies[61]. This observed phenomenon further supports the presence of a chromospheric resonance cavity, since it has been theoretically shown[62] that long-term modulating periods can be created in the confines of resonant filters. Secondly, the velocity amplitudes corresponding to the modelled ($\mathrm{rms} = 3.2$ km/s) and observed ($\mathrm{rms} = 3.5$ km/s) upper chromosphere are very similar, demonstrating that the wave amplification process is accurately accounted for in the Lare2D model. Finally, the spectral energies computed for both the modelled and observed time series show similar trends across regions I, II and III. In particular, the modelled region I also displays the relatively flat spectral energy that is consistent with the presence of evanescent waves. Next, the modelled region II reveals a similar peak wave energy at $\sim$5 mHz, followed by a gradual decline in spectral energy with a maximum-likelihood fitted gradient equal to -2.3 ± 0.3. As per the observed spectral gradients for region II (see the magenta data points in Fig. 3a), the modelled values also closely map to the presence of red noise (i.e., f^{-2}). Lastly, the modelled region III demonstrates an identical rise in spectral energy at $\sim$20 mHz ($\sim$50 s), before dropping off very rapidly with increasing frequency.

Importantly, however, is the fact that the blue data points in Fig. 3a indicate that the spectral slope associated with region III varies as a function of distance away from the umbral barycenter. Theoretical work[11] has revealed that the thickness of the chromospheric resonance cavity has implications for the steepness of the measured spectral gradient, with shallower resonance cavities demonstrating steeper spectral slopes than their thicker cavity counterparts. To investigate this

effect further, the thickness (i.e., atmospheric height span) of the resonance cavity was re-scaled at 80%, 90%, 110% and 120% of the original depth (Extended Data Fig. 4), providing the atmospheric parameters detailed in Extended Data Fig. 5. For each resonance cavity thickness, the numerical models were recomputed, with the spectral energies calculated and the corresponding spectral gradients measured using an identical maximum-likelihood approach. Utilising the stratified temperature profiles listed in Extended Data Fig. 5, the computed spectral slopes for region III can be plotted as a function of the magnetoacoustic wave propagation distances (Extended Data Fig. 6). It can be seen that larger wave propagation distances (i.e., increased cavity depths) introduce a greater resonant energy content, hence providing more energy across the frequency range, and thus reducing the steepness of the associated spectral slope.

The general trends depicted in Fig. 3 and Extended Data Fig. 6 are consistent with previous modelling efforts[11], whereby deeper resonance cavities produce inherently shallower spectral gradients in region III ($18 - 27$ mHz). Of course, it must be noted that Fig. 3 and Extended Data Fig. 6 depict the variations in the spectral slopes as a function of the distance over which the magnetoacoustic waves propagate. In an idealised case, where the magnetic fields are aligned with the normal to the solar surface, these propagation distances will be identical to the geometric height of the upper chromosphere. On the other hand, if the magnetic field lines are inclined to the solar normal, then this angle will need to be incorporated into the calculation to estimate the true geometric height of the upper chromosphere in that location. With this in mind, it becomes possible to estimate the depth of the chromospheric resonance cavity for each location within the sunspot umbra simply by comparing the measured spectral slope of region III to the reference spectral energies

computed via the Lare2D numerical models.

Here, we have utilised the presence of a spectral energy peak at $\sim$20 mHz (i.e., region III; see Fig. 2d) as an indicator of a resonance cavity existing in our observational and simulated data, which is consistent with theoretical and numerical investigations documented in recent years[9,11]. However, to confirm that a resonance cavity is the mechanism responsible for the elevated spectral energies in the range of $18-27$ mHz, we create an independent numerical test whereby the Lare2D simulations are re-run for a background atmosphere devoid of the steep transition region temperature gradient. For this test, the temperature reaches the chromospheric plateau value ($\sim$6000 K; see Extended Data Fig. 4) at an atmospheric height of 0 km, then remains constant through to the upper boundary of the simulation domain, hence removing the conditions necessary for an acoustic resonator to operate (i.e., the temperature gradient synonymous with the transition region).

The resulting spectral energies (Extended Data Fig. 7) reveal how removing the transition region entirely from the model atmosphere produces a shallower spectral gradient following the $\sim$5 mHz peak. This is likely a consequence of the flattened temperature profile modifying the acoustic cut-off frequency with atmospheric height, hence resulting in a different distribution of energies across the frequency spectrum[63]. Importantly, removing the steep temperature gradient inherent to the solar transition region, which is believed to be required for the initiation of resonance behaviour[9,11], acts to alleviate the rise in spectral energies at $\sim$20 mHz. As a result, we conclude that the heightened spectral energies contained within the observed and simulated region III ($18-27$ mHz; Fig. 2) are a direct consequence of the lower (photospheric) and upper (transition region) temperature gradients intrinsic to the solar atmosphere, hence giving rise to the

creation of a resonance cavity.

The range of gradients measured for region III ($18-27$ mHz) of the sunspot spectral energies span -5.4 ± 0.6 (close to the umbral barycenter) to -7.8 ± 0.6 (at the outermost extremities of the umbra). Immediately, this suggests that the chromospheric resonance cavity is thickest near the core of the umbra, dropping to its thinnest depth at the penumbral boundary. Extended Data Fig. 6 allows the wave propagation distance, $\tau_{\rm prop}$, to be defined as,

$$\tau_{\rm prop}\ ({\rm km}) = \frac{\text{Region III spectral slope} + 26.408}{0.009131}\ ,$$

where 0.009131 is the gradient of the dashed black line and 26.408 is the intercept on the y axis (Extended Data Fig. 6). The extreme values of the measured spectral slopes, -7.8 and -5.4, provide wave propagation distances on the order of 2035 km and 2300 km, respectively (shaded magenta and green regions in Extended Data Fig. 6).

However, the magnetic fields spanning the diameter of the sunspot umbral chromosphere are not all vertical in nature (Extended Data Fig. 8). Examining the magnetic field inclination angles, θ, derived from HAZEL inversions applied to the He I 10830 Å spectropolarimetric data reveals that the umbral cores have the most vertical magnetic fields (approximately 0 degrees), while the outermost extremities of the umbrae demonstrate the most inclined magnetic fields (approximately $35-50$ degrees on average). Furthermore, the filamentary structure that segregates the sunspot into two isolated umbrae displays increased inclination angles approaching 40 degrees (located at approximately 5.6 Mm along the FIRS slit in Extended Data Fig. 8).

As a result, the stratified wave propagation path lengths (Extended Data Fig. 4) are tilted

from the solar normal by the inclination angle, θ, which needs to be taken into consideration when estimating the true atmospheric height of the upper chromospheric boundary. As such, the true geometric height of the upper chromosphere, τ_{chromo}, can be defined as,

$$\tau_{\mathrm{chromo}}\,(\mathrm{km}) = \frac{\mathrm{Region\ III\ spectral\ slope} + 26.408}{0.009131}\cos\theta$$

$$= \tau_{\mathrm{prop}}\cos\theta\ .$$

Utilising the spatially-resolved inclination angles and spectral gradients provides true geometric heights of the upper boundary of the umbral cavity spanning 1300 ± 200 km (spectral slope of -7.8 ± 0.6 and an inclination angle of approximately 50 degrees; outer umbral edge) through to 2300 ± 250 km (spectral gradient of -5.4 ± 0.6 and a vertically-orientated magnetic field; umbral barycenter). This can be visualised graphically in Fig. 4, where the pink isocontours represent the geometric height of the upper chromospheric boundary across the diameter of the sunspot umbra.

Data Availability The data used in this paper are from the observing campaign entitled "*The influence of Magnetism on Solar and Stellar Atmospheric Dynamics*" (NSO-SP proposal T1081; Principle Investigator: D. B. Jess), which employed the ground-based Dunn Solar Telescope, USA, during July 2016. Additional supporting observations were obtained from the publicly available NASA's Solar Dynamics Observatory (https://sdo.gsfc.nasa.gov) data archive, which can be accessed via http://jsoc.stanford.edu/ajax/lookdata.html. The data that support the plots within this paper and other findings of this study are available from the corresponding author upon reasonable request.

26. Jess, D. B. *et al.* The Source of 3 Minute Magnetoacoustic Oscillations in Coronal Fans. *Astrophys. J.* **757**, 160 (2012).

27. Derks, A., Beck, C. & Martínez Pillet, V. Inferring telescope polarization properties through spectral lines without linear polarization. *Astron. Astrophys.* **615**, A22 (2018).

28. Cauzzi, G. *et al.* The solar chromosphere at high resolution with IBIS. I. New insights from the Ca II 854.2 nm line. *Astron. Astrophys.* **480**, 515–526 (2008).

29. Jess, D. B., Mathioudakis, M., Christian, D. J., Crockett, P. J. & Keenan, F. P. A Study of Magnetic Bright Points in the Na I D_1 Line. *Astrophys. J. Lett.* **719**, L134–L139 (2010).

30. Stangalini, M., Del Moro, D., Berrilli, F. & Jefferies, S. M. MHD wave transmission in the Sun's atmosphere. *Astron. Astrophys.* **534**, A65 (2011).

31. Lagg, A., Woch, J., Solanki, S. K. & Krupp, N. Supersonic downflows in the vicinity of a growing pore. Evidence of unresolved magnetic fine structure at chromospheric heights. *Astron. Astrophys.* **462**, 1147–1155 (2007).

32. Aznar Cuadrado, R., Solanki, S. K. & Lagg, A. Velocity distribution of chromospheric downflows. In Kneer, F., Puschmann, K. G. & Wittmann, A. D. (eds.) *Modern solar facilities - advanced solar science*, 173 (2007).

33. González Manrique, S. J. *et al.* Fitting peculiar spectral profiles in He I 10830Å absorption features. *Astronomische Nachrichten* **337**, 1057 (2016).

34. González Manrique, S. J. *et al.* Temporal evolution of arch filaments as seen in He I 10 830 Å. *Astron. Astrophys.* **617**, A55 (2018).

35. Zaghloul, M. R. On the calculation of the Voigt line profile: a single proper integral with a damped sine integrand. *Mon. Not. R. Astron. Soc.* **375**, 1043–1048 (2007).

36. Henriques, V. M. J. *et al.* Stable umbral chromospheric structures. *Astron. Astrophys.* **574**, A131 (2015).

37. Bel, N. & Leroy, B. Analytical Study of Magnetoacoustic Gravity Waves. *Astron. Astrophys.* **55**, 239 (1977).

38. Roberts, B. MHD Waves in the Solar Atmosphere. In Lacoste, H. (ed.) *SOHO 13 Waves, Oscillations and Small-Scale Transients Events in the Solar Atmosphere: Joint View from SOHO and TRACE*, vol. 547 of *ESA Special Publication*, 1 (2004).

39. Löhner-Böttcher, J., Bello González, N. & Schmidt, W. Magnetic field reconstruction based on sunspot oscillations. *Astronomische Nachrichten* **337**, 1040 (2016).

40. Jess, D. B. *et al.* Solar coronal magnetic fields derived using seismology techniques applied to omnipresent sunspot waves. *Nature Physics* **12**, 179–185 (2016).

41. Jess, D. B. *et al.* An Inside Look at Sunspot Oscillations with Higher Azimuthal Wavenumbers. *Astrophys. J.* **842**, 59 (2017).

42. Krishna Prasad, S. *et al.* The Frequency-dependent Damping of Slow Magnetoacoustic Waves in a Sunspot Umbral Atmosphere. *Astrophys. J.* **847**, 5 (2017).

43. Groth, E. J. Probability distributions related to power spectra. *Astrophys. J. Supp.* **29**, 285–302 (1975).

44. Papadakis, I. E. & Lawrence, A. Improved Methods for Power Spectrum Modelling of Red Noise. *Mon. Not. R. Astron. Soc.* **261**, 612 (1993).

45. Morton, R. J., Weberg, M. J. & McLaughlin, J. A. A basal contribution from p-modes to the Alfvénic wave flux in the Sun's corona. *Nature Astronomy* (2019).

46. Matthaeus, W. H. *et al.* Density and Magnetic Field Signatures of Interplanetary 1/f Noise. *Astrophys. J. Lett.* **657**, L121–L124 (2007).

47. Huang, S. Y., Hadid, L. Z., Sahraoui, F., Yuan, Z. G. & Deng, X. H. On the Existence of the Kolmogorov Inertial Range in the Terrestrial Magnetosheath Turbulence. *Astrophys. J. Lett.* **836**, L10 (2017).

48. Sheikholeslami, M., Abelman, S. & Ganji, D. D. Numerical simulation of mhd nanofluid flow and heat transfer considering viscous dissipation. *International Journal of Heat and Mass Transfer* **79**, 212 – 222 (2014).

49. Goldstein, M. L., Roberts, D. A. & Fitch, C. A. Properties of the fluctuating magnetic helicity in the inertial and dissipation ranges of solar wind turbulence. *J. Geophys. Res.* **99**, 11519–11538 (1994).

50. Maltby, P. *et al.* A new sunspot umbral model and its variation with the solar cycle. *Astrophys. J.* **306**, 284–303 (1986).

51. Avrett, E. H. & Loeser, R. Models of the Solar Chromosphere and Transition Region from SUMER and HRTS Observations: Formation of the Extreme-Ultraviolet Spectrum of Hydrogen, Carbon, and Oxygen. *Astrophys. J. Supp.* **175**, 229–276 (2008).

52. Borrero, J. M. *et al.* VFISV: Very Fast Inversion of the Stokes Vector for the Helioseismic and Magnetic Imager. *Sol. Phys.* **273**, 267–293 (2011).

53. Schou, J. *et al.* Design and Ground Calibration of the Helioseismic and Magnetic Imager (HMI) Instrument on the Solar Dynamics Observatory (SDO). *Sol. Phys.* **275**, 229–259 (2012).

54. Rabello-Soares, M. C., Roca Cortes, T., Jimenez, A., Andersen, B. N. & Appourchaux, T. An estimate of the solar background irradiance power spectrum. *Astron. Astrophys.* **318**, 970–974 (1997).

55. González Manrique, S. J., Kuckein, C. & Ruiz Cobo, B. Comparison of bisectors with inversions based on response functions to infer line-of-sight velocities on the Si I 10827Å. *Astron. Astrophys.* (2019).

56. Felipe, T., Khomenko, E., Collados, M. & Beck, C. Multi-layer Study of Wave Propagation in Sunspots. *Astrophys. J.* **722**, 131–144 (2010).

57. Vernazza, J. E., Avrett, E. H. & Loeser, R. Structure of the solar chromosphere. III - Models of the EUV brightness components of the quiet-sun. *Astrophys. J. Supp.* **45**, 635–725 (1981).

58. Centeno, R., Collados, M. & Trujillo Bueno, J. Spectropolarimetric Investigation of the Propagation of Magnetoacoustic Waves and Shock Formation in Sunspot Atmospheres. *Astrophys. J.* **640**, 1153–1162 (2006).

59. Centeno, R., Collados, M. & Trujillo Bueno, J. Wave Propagation and Shock Formation in Different Magnetic Structures. *Astrophys. J.* **692**, 1211–1220 (2009).

60. Krishna Prasad, S., Jess, D. B. & Khomenko, E. On the Source of Propagating Slow Magnetoacoustic Waves in Sunspots. *Astrophys. J. Lett.* **812**, L15 (2015).

61. Marsh, M. S. & Walsh, R. W. p-Mode Propagation through the Transition Region into the Solar Corona. I. Observations. *Astrophys. J.* **643**, 540–548 (2006).

62. Zhukov, V. I. Oscillations on the Sun in regions with a vertical magnetic field. II. On the calculation of the sunspot umbral oscillations. *Astron. Astrophys.* **433**, 1127–1132 (2005).

63. Zhugzhda, Y. D. Three-minute oscillations in sunspots: Seismology of sunspot atmospheres. *Astronomy Letters* **33**, 622–643 (2007).

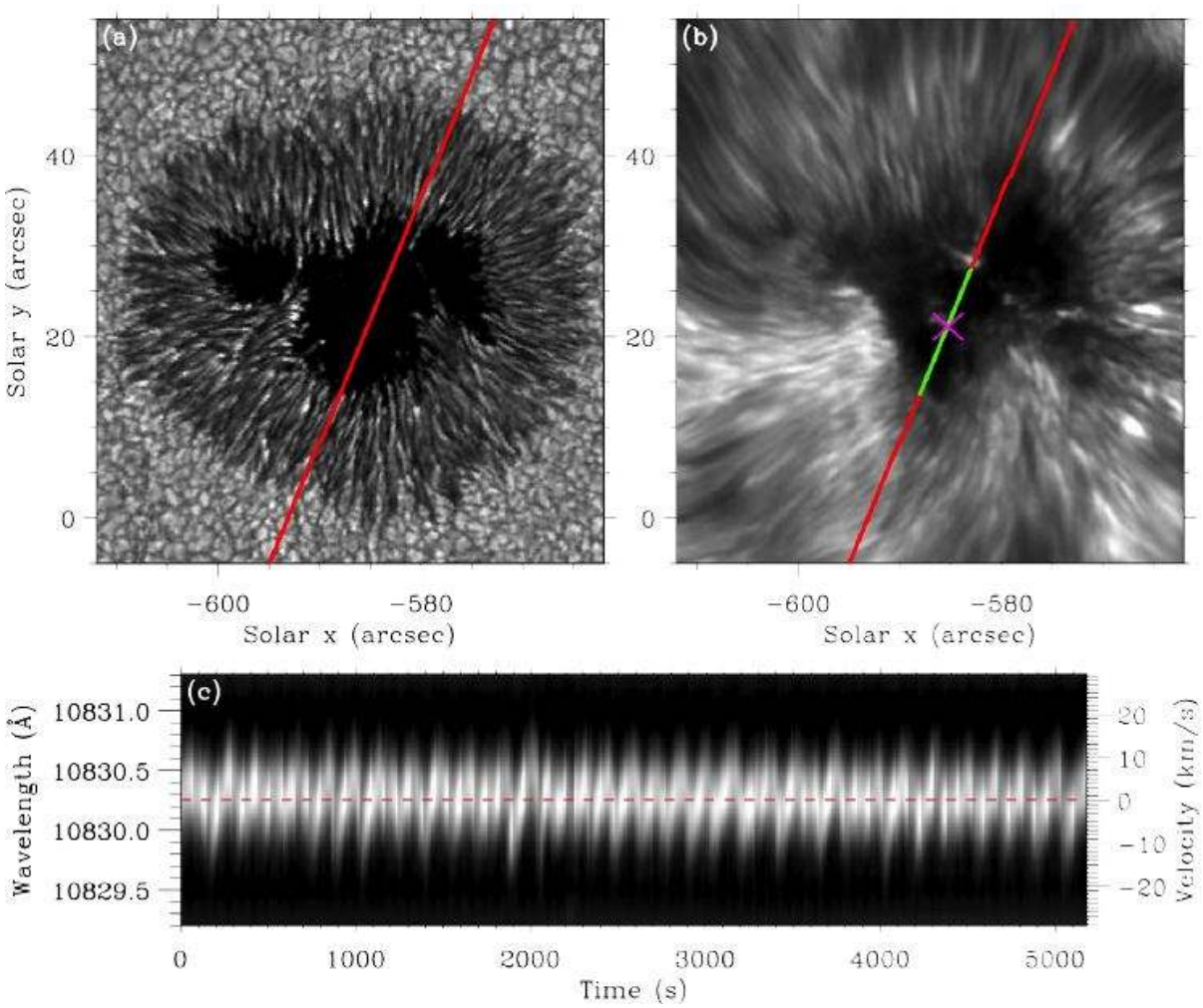

Figure 1

The velocity signatures of the magnetised sunspot atmosphere observed on 14 July 2016.

(a & b) ROSA 4170 Å continuum (photosphere) and IBIS 8542 Å line core (chromosphere) images of the sunspot atmosphere at 13:42 UT on 14 July 2016, with the axes displaying the associated heliocentric co-ordinates. The solid red lines highlight the position of the FIRS slit, while the solid green line indicates the portion of the slit that clearly crosses the chromospheric umbra (i.e., not overlapping with penumbra or quiet Sun structures). The pink cross identifies a persistent umbral brightening that segregates the umbral spectra into two distinct regions.

(c) A velocity-time image that documents the spectral and temporal evolution of the He I 10830 Å Stokes I line profile from a single umbral pixel. The black-to-white colour scale represents the inverted spectral intensities to assist with visual clarity, while the horizontal dashed red line indicates the rest position of the He I 10830 Å line core.

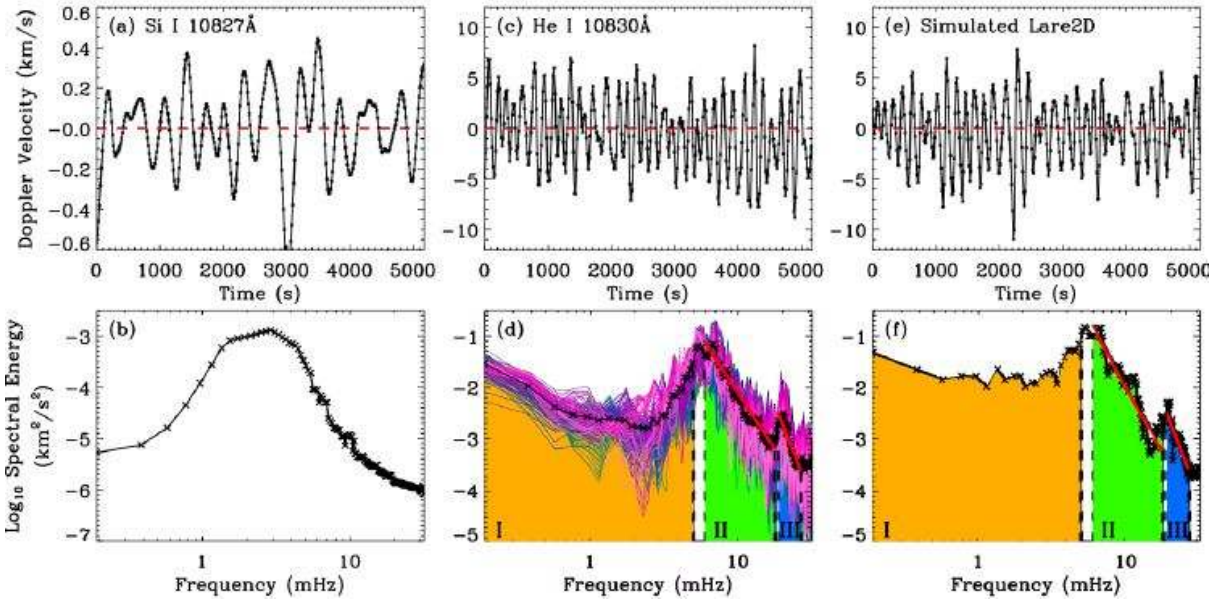

Figure 2

Doppler velocities and spectral energies of observed and simulated time series.

(a & b) The Si I 10827 Å (photospheric) Doppler velocity signal for an umbral pixel, with its corresponding spectral energy displayed on log–log axes.

(c) The co-spatial He I 10830 Å (upper chromospheric) Doppler velocity signal, where higher frequency waves are more readily visible when compared to panel (a).

(d) The calculated He I 10830 Å spectral energies, where the graduated blue-to-pink coloured lines represent spectra derived across the entire sunspot umbral diameter. The solid black line represents the average umbral spectral energy.

(e & f) The simulated velocity time series, which is extracted from the Lare2D computational domain at an atmospheric height that is compatible with the formation of the He I 10830 Å spectral line, along with its corresponding spectral energy. The dashed red lines, panels (a), (c) and (e), highlight a zero velocity for visual reference. Orange, green and blue shaded regions (bounded by black vertical dashed lines; panels (d) and (f) isolate the spectral energies into regions I (< 5 mHz), II (6 – 17 mHz) and III (18 – 27 mHz). The solid red lines, panels (d and (f), highlight the respective maximum-likelihood fits spanning the frequency domains corresponding to regions II and III.

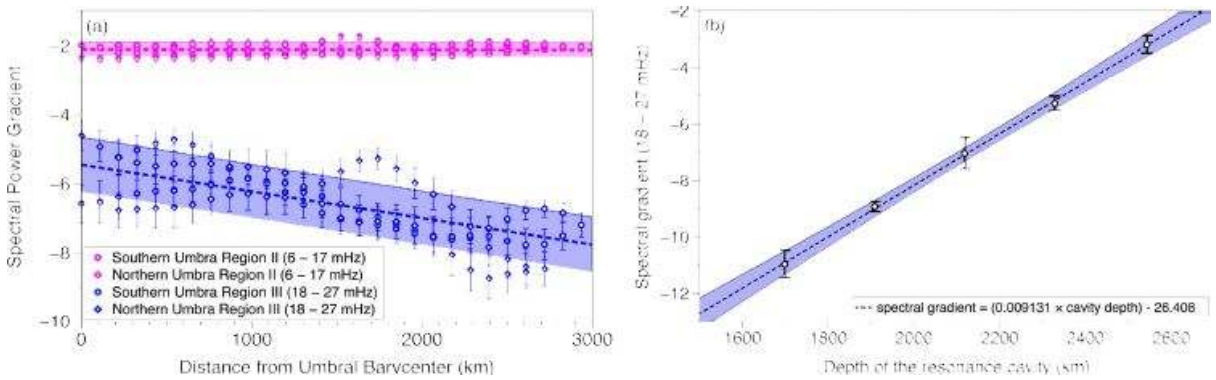

Figure 3

Spectral energy gradients of observed and simulated time series.

(a) The spectral power gradients measured for each of the umbral Fourier energy densities, displayed as a function of distance from their associated umbral region barycenter. Here, the magenta and blue colours correspond to regions II (6 – 17 mHz) and III (18 – 27 mHz), while the circle and diamond symbols relate to the southward and northward locations in relation to the persistent umbral brightening, respectively. The vertical error bars placed on each data point correspond to the maximum-likelihood 1σ fitment uncertainties when measuring the spectral power-law gradients. The dashed magenta and blue lines highlight the linear lines of best fit associated with regions II and III, while the shaded magenta and blue regions identify the standard deviations for the lines of best fit, respectively.

(b) The spectral slopes of region III (18 – 27 mHz), which are calculated from the maximum-likelihood fitments of the Fourier spectral energies produced by Lare2D numerical simulations, as a function of the variable resonance cavity depths imposed in the modelled atmospheres. The vertical error bars highlight the maximum-likelihood 1□ fitment uncertainties achieved when measuring the corresponding spectral power-law gradients. The dashed black line maps the linear best-fit line through the data points, while the blue shaded region (bounded by the black dotted lines) highlights the 95% confidence level associated with the fitted line.

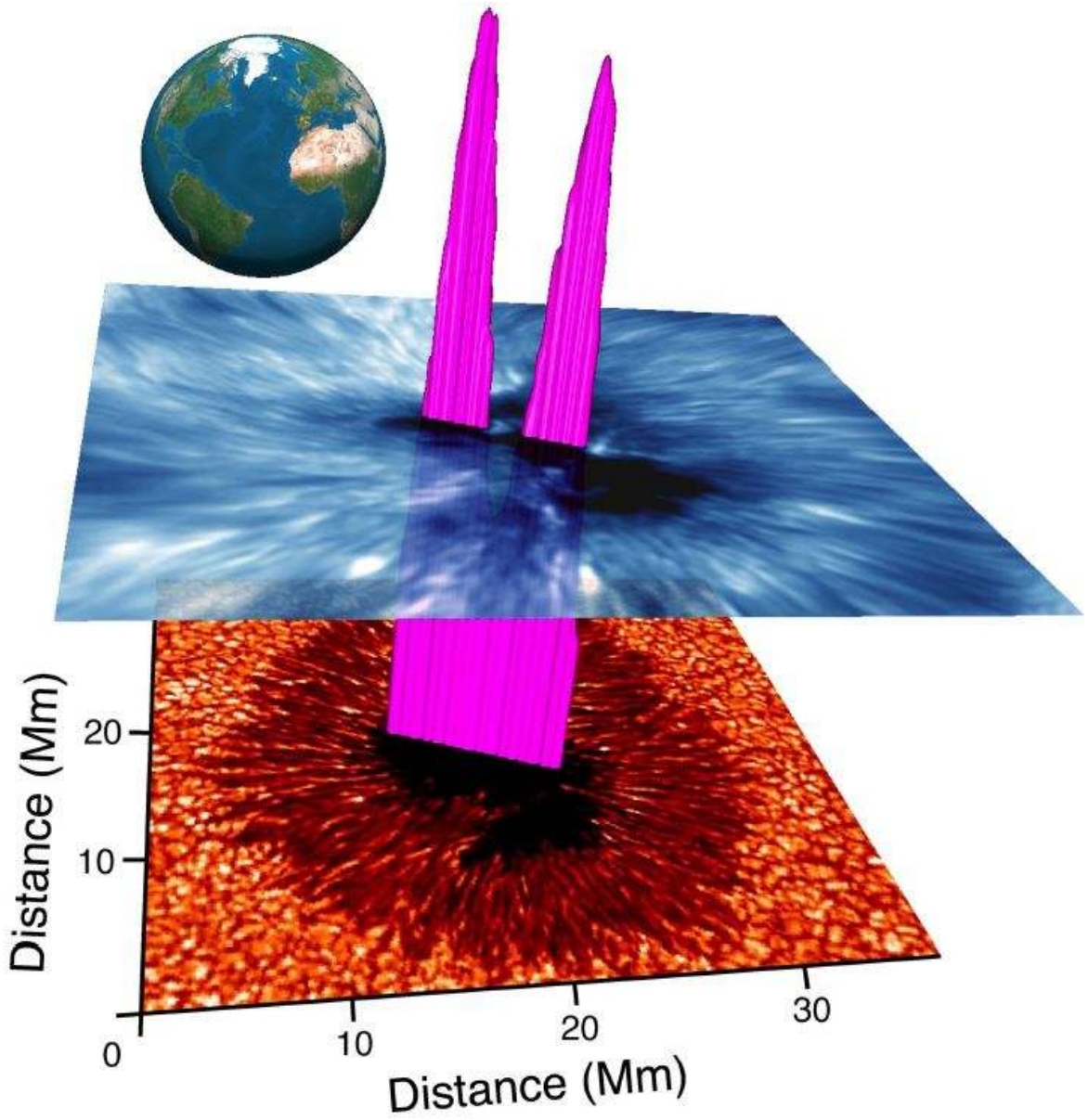

Figure 4

Three-dimensional visualisation of the geometric extent of the chromosphere above active region NOAA 12565.

The geometric extent of the chromosphere, visualised here as the pink isocontours extending upwards from the photospheric (ROSA 4170 Å continuum) umbra and through the chromospheric (IBIS 8542 Å line core). It can be seen that the depth of the resonance cavity is suppressed in the immediate vicinity of the trans-umbral filamentary structure, providing geometric heights of approximately 1300 km, which is consistent with the depth measured at the outermost edges of the umbra. The cores of the umbrae display the largest resonance cavity depths, often with geometric heights on the order of 2300 km. An image of the Earth is added to provide a sense of scale.

Note: The pink resonance cavity depth contours are not to scale.